International Journal of Automotive Technology, Vol. 22, No. 2, pp. 403–414 (2021)
DOI 10.1007/s12239–021–0038–y

pISSN 1229–9138/ eISSN 1976–3832

IMPINGEMENT-INDUCED STABILITY ANALYSIS OF INTAKE MANIFOLD AIR JETS USING HIGH SPEED PIV AND POD

Penghui Ge[1)] and David Ling-Shun Hung[1,2)*]

[1)]University of Michigan-Shanghai Jiao Tong University Joint Institute, Shanghai Jiao Tong University, Shanghai 200240, China
[2)]National Engineering Laboratory for Automotive Electronic Control Technology, School of Mechanical Engineering, Shanghai Jiao Tong University, Shanghai 200240, China

(Received 11 February 2020; Revised 19 May 2020; Accepted 20 June 2020)

ABSTRACT–The flow stability induced by the impingement of gas jets exiting from the intake manifold affects the in-cylinder flow characteristics of internal combustion engine. Using high-speed planar particle image velocimetry (PIV) with proper orthogonal decomposition (POD) analysis, an investigation was conducted to reveal the spatio-temporal characteristics of annular gas jets impinging in a region between the exits of two intake valves. Unique flow behaviors are identified where strong initial interaction of impinging jets appears near the valve exit as a result of fierce flow vorticity competition in both clockwise and counter-clockwise directions. This mixing zone exhibits strong fluctuations in the angle of the merged gas jet. Flow vorticity and merged jet angle are highly correlated with each other, and the quasi-periodical behavior of the jet impingement is linked to the kinetic energy dissipation. In addition, using POD, the underlying flow structures show large-scale rotating structures with translation which are responsible for the quasi-periodical behavior. In summary, three types of flow stability can be identified resulting from different levels of induced impingement: one-way interaction of single jet flow case, two-way interaction of dual impinging jets with equal flow magnitude, and transitional one-way interaction of dual impinging jets with unequal flow magnitude.

KEY WORDS : Intake manifold air jets, Stability, Vorticity, Jet direction, Underlying flow structure

1. INTRODUCTION

The interactions of multiple gas jets and their mixing characteristics are critical in a wide range of flow processes in chemical, automotive, and pharmaceutical applications. Such interaction usually creates highly transient and complex flow structures which are constrained by physical configuration of the ambient environment. A perfect example can be found in the intake air flow process of an internal combustion engine (Xu *et al*., 2016). During the intake stroke, intake valves are opening while the piston is moving towards the bottom dead center of the combustion cylinder. The downward movement of piston top increases the cylinder volume and therefore reduces the cylinder pressure to sub-atmospheric condition. Pressure difference draws fresh air along the intake ports into the cylinder through the annular gaps of intake valves. Air exiting the valve gaps merges and creates highly transient complex flow structures such as vortices of multiple length scales in the cylinder (from micrometers to centimeters) (Borée and Miles, 2014; Voisine *et al*., 2010; Ohm, 2013). Large-scale tumble air motion is strongly affected by the intake air charging process (Brusiani *et al.*, 2014). Fuel film deposition caused by the presence of large-scale air flow carrying small droplets towards cylinder wall should be mitigated (Frapolli *et al.*, 2019). In addition, governing the initial jet direction during intake stroke can affect burning rate and heat release during combustion process (Ohm, 2013). Therefore, it is necessary to investigate the intake air process which can help elucidate the fuel-air mixing or combustion behaviors that typically occur much later in the engine cycle. Another example can be found in natural gas engine where the interaction between fresh intake air and gaseous fuel constitutes a "multiple-component single-phase" mixing process. It is clear that an improved fuel-air distribution impacts the emission and combustion efficiency in a positive way (McTaggart-Cowan *et al*., 2010). Therefore, detail spatio-temporal characterizations of the impingement-induced flow stabilities of gas jets in a constrained environment have remained as a critical research area for decades.

Many researchers have used pointwise measurement techniques such as laser Doppler anemometry (Wang *et al*., 2016) and hot-wire anemometry (Ko and Lau, 1989) to investigate the flow fields at specific locations. Both

*Corresponding author. e-mail: dhung@sjtu.edu.cn

techniques are known to provide highly temporal data of local mean flow and velocity fluctuations which are often used for frequency spectral analysis. Even though the measurements can be repeated at multiple locations within the flow field, it is quite a challenge to achieve a holistic view of detail flow structures, especially when there exist strong temporal and cycle-to-cycle variations. While computational fluid dynamics calculations with large eddy simulation models have been widely applied to predict in-cylinder flow field, the model accuracy still requires a tremendous quantity of high-resolution experimental flow data in both temporal and spatial domains for model validations (Li *et al*., 2019).

Recently, time-resolved particle image velocimetry (PIV) technique has become a primary diagnostic tool to investigate the transient planar flow fields with detail temporal and spatial information (Hribernik, *et al*., 2019; Lee and Hassan, 2018; Yin *et al*., 2019). For the intake flow field measurements in an engine with full optical access to its combustion cylinder (also known as an optical engine), PIV has been used almost exclusively in engine flow field research. One common measurement location is through a vertical plane which is aligned with the diameter of both intake and exhaust valves. As air enters through the valve gap, this plane provides the most characteristic two-dimensional flow field pattern with minimum out-of-plane motion. Previous studies have shown that a free jet from a nozzle can be characterized by three representative regions: initial region, transition region, and fully-developed region (Shim *et al*., 2013). The initial region is at the vicinity of nozzle exit and is characterized by an irrotational jet core surrounded by shear layer. The velocity in the jet core is almost equal to the jet exit velocity, which is also unstable due to the Kelvin-Helmholtz instability mechanism (Ho and Huerre, 1984; Shim *et al*., 2013). Such instability will grow with downstream distance to roll up into small vortices. In addition, shear layer around the jet core merges at the end of initial region and a transition region is thus formed. After that, the jet reaches a dynamic equilibrium state in a fully developed region. Using proper orthogonal decomposition (POD) and spectral analysis, Shim *et al*. (2013) concluded that the symmetrical counter-rotating vortical structures with different characteristic frequencies formed in initial region remained as jet developed downstream. A strong correlation among the three regions was identified.

Interactions of counter-flowing jet pairs (Saghravani and Ramamurthy, 2010; Sivapragasam *et al*., 2014; Xia and Zhong, 2017) and parallel-flowing jet pairs (Lee and Hassan, 2018; Li *et al*., 2019; Nasr and Lai, 2010) facilitate momentum and mass exchanges. For instance, Saghravani and Ramamurthy (2010) identified a spatial feature of jet penetration under dual counter-flowing jets. In their study, they found that jet penetration was an important quantity since it affected the zone of momentum and mass transfer. It was revealed that the jet penetration length was linearly correlated with the ratio of initial jet velocity. Parallel jets are widely applied to increase the multiple-component single-phase mixing efficiency. Lee and Hassan (2018) identified the underlying modes of dual parallel jets interaction using POD method. The interaction and transport of multi-scale vortical structures were visualized. The frequency spectrum revealed that lower frequencies dominated the flow behavior as jets moved downstream. The reason for the change of dominant frequencies is attributed to the vortex development downstream. In addition, Li *et al*. (2007) studied the impingement of dual parallel jets on a flat plate and analyzed the unsteadiness near the impingement region using spectral frequency analysis. They found that small eddies from the plate were fed into the region between two jets which enhanced the unsteadiness of jet shear layer. However, the large fluctuations with higher local peaks in energy spectrum occurred at the location closest to the plate. Yin *et al*. (2019) used POD to extract the coherent structures of triple interacting buoyant gas plumes formed by three identical rectangular blocks. The coherent structures were identified as large-scale outer-side vortex ring and shear-layer vortex shedding, which dominated the interaction process.

The scope of this study is to elucidate the flow stability of intake manifold air jets induced by their impinging interactions at the valve exit region. Figure 1 depicts the zone of interaction in the vicinity of the two adjacent valves which are in close proximity to each other. Although the annular jet flow shows three-dimensional behavior, the middle plane sectioning through the diameter of both valves is primarily dominated by two-dimensional motion. The interacting zone in the vicinity of both intake valves along this middle plane should exhibit minimum out-of-plane motion. Such middle representative plane shows the strongest interaction in a two-dimensional manner, and therefore this middle section plane is selected for detail planar PIV measurements in this study. The flow behavior in the field of view (FOV) on the right side of Figure 1 illustrates the flow domain of this investigation. The FOV reveals the initial interaction as two annular jets contact

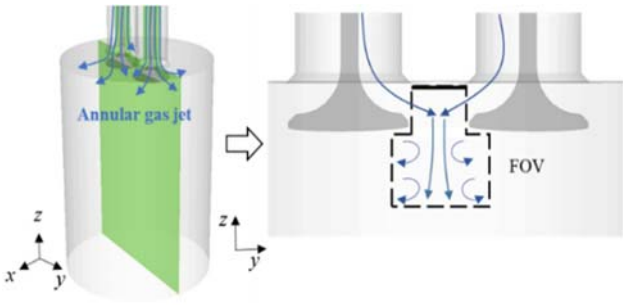

Figure 1. Illustration of FOV of interest in valve exit region.

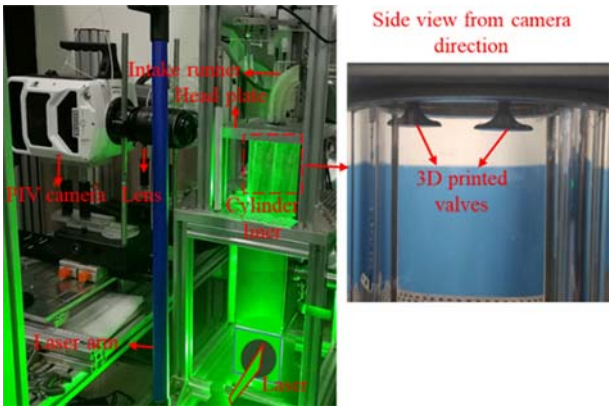

Figure 2. Experimental setup with a magnified view inside the measurement flow domain.

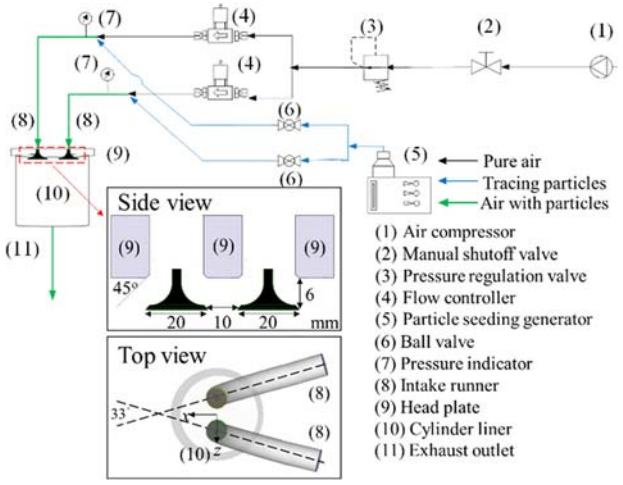

Figure 3. Schematic of dual-valve flow system with valve configuration dimensions.

with each other and their merging behavior.

2. EXPERIMENTAL SETUP AND PIV FLOW MEASUREMENTS

Figure 2 depicts the experimental test rig. The valve configuration on the right side mimicked a practical dual-valve intake configuration commonly found in an internal combustion engine. A dual-cavity high-speed laser (Photonics, Nd:YLF) and a high-speed PIV camera Phantom V1210 with a Nikon 105 mm camera lens were used to facilitate the planar PIV measurements. Two laser beams from their corresponding laser heads were optically combined into a single laser sheet with a thickness of 1 mm. The laser sheet was reflected by a 45-degree mirror to illuminate the measurement plane through the mid-section of the valves in the cylinder with a diameter of 86 mm. The high-speed camera was located perpendicular to the measurement plane. The details of PIV setup are summarized in Table 1.

As shown in Figure 3, the test setup included two separate air flow paths leading to the cylinder which was connected through a common head plate. The volumetric flow rates were independently controlled by two digital flow controllers with an accuracy of 0.1 %. Compressed air was fed into two intake runners in separate paths of roughly equal length. The difference percentage of the two intake runners in terms of flow rates is less than 2 % after swapping intake valves. The angle between the two intake runners was 33 degrees. The valves were made with photosensitive resin using a 3D printing process to mimic the real intake valves used in internal combustion engine. The valve seat angle was 45 degrees. The valve lift was kept at 6 mm. The valve face diameter was 20 mm and the minimum gap between the edges of two valves was 10 mm. The two valves were vertically installed which was parallel to the cylinder axis. The flow exit was open to atmosphere, allowing the air-particle mixture to be directly discharged outside through an exhaust outlet on the bottom of the test-rig.

In this study, single-valve and dual-valve conditions were used to generate the gas jet interaction process. For each valve, the gas bulk flow velocity in the corresponding intake runner was based on the volumetric flow rate divided by the cross-section area of the intake runner. Three conditions with bulk flow magnitude ratios of 0.0, 1.0, and 2.2 were investigated, as tabulated in Table 2. A bulk flow magnitude ratio of 0.0 represents the baseline case where only a single free jet is formed. The other two conditions show different

Table 1. Key parameters of PIV setup.

Item	Camera/laser frequency (kHz)	Laser energy (mJ/pulse)	Time interval between two laser pulses (μs)
Value	1	30	100

Table 2. Gas bulk flow velocity in the intake runners and velocity ratios.

Description		Value		
Gas bulk flow velocity in intake runner (m/s)	Left runner	5.0	5.0	5.0
	Right runner	0.0	5.0	11.0
Bulk flow velocity ratio, ε (right/left)		0.0	1.0	2.2

levels of interaction between two annular jets. The corresponding Reynolds numbers in the intake runner are 5912 and 13007 for bulk flow velocities of 5 m/s and 11 m/s, respectively.

A particle generator was used to supply the seeding particles into the intake runners for PIV measurements. To ensure optimal seeding density for PIV measurements along each path, a ball valve was used to control the amount of seeding particles added to the flow path. It is important to select the seeding particles which are capable of following the air flow closely. Therefore, seeding particles should be as small as possible. On the contrary, particles should also be large enough to scatter adequate light (Mie) signal for PIV measurements. Therefore, balancing these two factors can be made by considering the non-dimensional Stokes number (*Stk*) which was calculated to be 0.0013 (much lower than 1.0). Therefore, the silicone oil particles were able to follow the flow well. The particle motion captured by the image cross-correlation can accurately reflect the real gas jet velocity. With high-quality particle images, the pixels of the entire raw image were partitioned into small grids using an interrogation window of 32 pixels by 32 pixels. The overlapping percentage of interrogation windows was set to 50 %, resulting in 51 vectors within a spatial length of 10 mm. It is possible that the velocity vector map may contain outlier and noise vectors from weak image correlation. To remove these outlier vectors, a post-processing step with Gaussian weight function was applied to the interrogation windows to improve the data accuracy. A threshold peak ratio of 1.3 between the first peak and the second peak was selected to eliminate any vector with a weak correlation. A median filter was applied to remove the spurious vectors with locally large deviations compared to their neighboring vectors. Finally, an interpolation procedure was used to fill the spatial grids where the vectors were missing. In this study, the spatial resolution was 0.2 mm and the maximum measurement uncertainty of flow vectors is 0.3 m/s in the *y*-axis and 0.2 m/s in the *z*-axis.

3. FLOW ANALYSIS METHODS

3.1. Impinging Gas Jet Interaction Characteristics

The kinetic energy (KE) of gas jet represents the energy of its motion. The interaction of gas jets accompanies with KE dissipation due to gas intramolecular friction. Since the KE distribution is a zone-related phenomenon as a result of interaction, the investigated FOV is divided into two specific sub-zones in the valve exit region as marked in Figure 4. Zone 1 is the top domain of FOV and Zone 2 is below zone 1. These two zones have the same dimensions (10 mm × 7 mm) and the total number of velocity vector (51 × 36) for each zone. The total specific KE calculation of each zone is the sum of specific KE of all velocity vectors inside the zone itself. The total specific KE in the two zones is named by KE_{zone1} and KE_{zone2} respectively. The

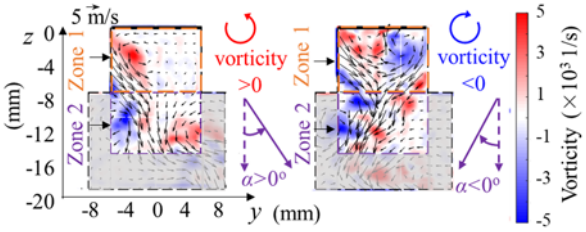

Figure 4. Illustration of two sub-zones, counterclockwise vorticity, clockwise vorticity and overall jet angle (flow fields are displayed at an interval of 5 vectors).

combined specific KE ($KE_{zone1,2}$) is the sum of KE_{zone1} and KE_{zone2}.

In addition, when two jets impinge at each other after exiting shortly from their annular valve nozzles, the initial merging and subsequent mixing behavior are two important criteria for gauging the flow characteristics. Therefore, zone 1 reveals the initial interaction when two jets contact with each other, and zone 2 illustrates their mixing characteristics. Since two jets meet at a location aligned with the valve seat angle, the momentum balance of both jets creates an initial contact zone with a strong flow rotational structure (flow vorticity) which is a good indicator of initial merging behavior. This merging behavior continues to evolve into a clear jet with a specific direction (angle) in zone 2. As expected, this jet angle in zone 2 is closely related to the flow vorticity in zone 1. Therefore, both flow vorticity and merged jet angle are important parameters in this study.

The vorticity represents the rotation strength of a continuum at a specific point. As shown in Figure 4, clockwise vorticity is considered negative and vice versa. A global vorticity value based on the rotation strength within a zone can be further divided into $\vec{\omega}_{pos}$ (the sum of positive vorticity) and $\vec{\omega}_{neg}$ (the sum of negative vorticity). The total vorticity $\vec{\omega}$ is the sum of $\vec{\omega}_{pos}$ and $\vec{\omega}_{neg}$. The sum of positive or negative vorticity is a good indicator to represent either counterclockwise or clockwise rotation strength within a certain zone (zone 1 in this study). The total vorticity is useful to estimate the dominant direction of rotation. The second important parameter is the overall angle of the merged jet. The angle definition is shown in Figure 4.

Similar to the sum of vorticity, a global value is defined to represent the merged jet angle. The overall jet angle α in zone 2 is calculated as follows:

$$\alpha = \frac{1}{L}\sum_{l=1}^{L} \alpha_l p_l \tag{1}$$

where l is the l^{th} vector among the total vector number L in zone 2, α_l is the angle of the l^{th} vector. Based on the measurement uncertainty of flow vectors, the uncertainty of α_l is estimated to be +/– one degree. However, the flow magnitude of some vectors is much smaller and these vectors should contribute less to the direction of overall jet

angle. Thus, a weighted coefficient p_l relative to the flow magnitude of each flow vector is defined:

$$p_l = \frac{\sqrt{(v_l^2 + w_l^2)}}{\max(\sqrt{(v^2 + w^2)_{zone2}})} \tag{2}$$

where v_l and w_l are the components of the l^{th} vector in the y and z axes, $\max(\sqrt{(v^2+w^2)_{zone2}})$ is the maximum flow magnitude inside zone 2.

3.2. Proper Orthogonal Decomposition

A brief overview of POD is presented here. The POD has been applied in flow analysis to identify variations among a series of flow snapshots. This method extracts the underlying modes in the priority of spatial correlations (Chen *et al*., 2012; Fogleman *et al*., 2004; Liu *et al*., 2013; Qin *et al*., 2019). Similar to the previous POD procedure undertaken by Chen *et al.* (2012) and Chatterjee (2000), in this study, the flow velocity mean is not subtracted from the snapshots prior to the application of POD. Using POD, the flow fields u^k (k = 1, 2, …, K) are decomposed into mode coefficients c_m^k (m = 1, 2, …, M) and spatial components φ_m which are orthogonal to each other. The superscript index k represents the k^{th} flow field and the total number of inputting flow fields is K. φ_m is the spatial basis function known as POD mode structure, and M is the finite number of basis functions, that is equal to the total number of snapshots, $M \equiv K$. When these components are linearly combined, the original flow fields u^k are expected to be reconstructed such that:

$$u^k = \sum_{m=1}^{M} c_m^k \varphi_m \tag{3}$$

Thus, the objective here is to achieve u^k for any j(j = 1, 2, …, M):

$$\min \left\| u^k - \sum_{i=1}^{j} c_i^k \varphi_i \right\| \tag{4}$$

where $\| \|$ denotes the L^2 normal. The orthogonality of POD modes is represented by the following equation:

$$\varphi_i \varphi_j^T = \begin{cases} 0 & if\ i \neq j \\ 1 & if\ i = j \end{cases} \tag{5}$$

These two constraint equations can be satisfied by solving the eigenvalue problem of correlation matrix UU^T / K of flow fields:

$$\left(\frac{UU^T}{K} \right) \beta = \lambda \beta \tag{6}$$

$$U = [u^1, u^2, ..., u^k, ..., u^K] \tag{7}$$

The singular value decomposition of the correlation matrix is adopted to achieve the eigenvalues and eigenvectors. These eigenvalues are in decreasing order and represent the kinetic energy content of modes. Through projecting the snapshot matrix U onto the eigenvectors and then normalized by themselves, the modes can be achieved. Thus, these modes contain structure information rather than kinetic energy content. The mode coefficients are calculated by projecting the snapshot matrix U onto the normalized modes again. The detail calculations can be found in reference (Chen *et al*., 2012). Accordingly, the kinetic energy KE_m and kinetic energy percentage KEP_m of modes are defined using the following equations:

$$KE_m = \frac{1}{2} \sum_{k=1}^{K} (c_m^k)^2 \tag{8}$$

$$KEP_m = \frac{KE_m}{\sum_{m=1}^{M} KE_m} \times 100\% \tag{9}$$

where m denotes mode number and its range is from 1 to 100 in this study. These modes are ordered from the largest kinetic energy to the lowest kinetic energy. The distribution of kinetic energy percentage reflects the fluctuations of flow fields. The modes are further analyzed to determine the underlying flow structures of the gas jet interactions.

4. RESULTS AND DISCUSSIONS

4.1. Spatio-Temporal Characteristics of Gas Jet Interaction Analysis of the Original In-Cylinder Flow Fields

The individual snapshots are first used to visualize the instability of flow structures associated with the gas bulk flow condition in intake runners. Figure 5 shows four consecutive snapshots with an interval time of 2 ms and the 100-cycle average flow structure. The single jet flow behavior of the 5 vs 0 m/s condition is depicted in Figure 5 (a) which is regarded as the baseline condition. From the average flow filed, a single jet is developed and its direction is aligned well with the valve seat angle. When the jet flows through a stagnant environment, the velocity gradient exists near their interface. Individual snapshots show flow instability and small eddies are found near the jet boundary as this single jet continues to emerge from zone 1 to zone 2. Such a velocity gradient leads to the generation of small eddies and entrainment from the surrounding. This observation is in accordance with the Kelvin-Helmholtz instability.

When both valves are open, the flow phenomena are very different than the single jet situation. As depicted in Figure 5 (b), the gas bulk flow velocities are equal to 5 m/s in both intake runners. That means the kinetic energy of both jets is similar. However, their momentum directions are opposite in the y-axis, resulting in the momentum loss at the impinging point. From the average flow of 5 vs 5 m/s condition, two symmetric rotating structures are observed in zone 1 as two distinct jets are formed after exiting the valve. Such rotating structures of initial interaction between two impinging jets generate an enhanced entrainment process. The reason for vortex formation can be found

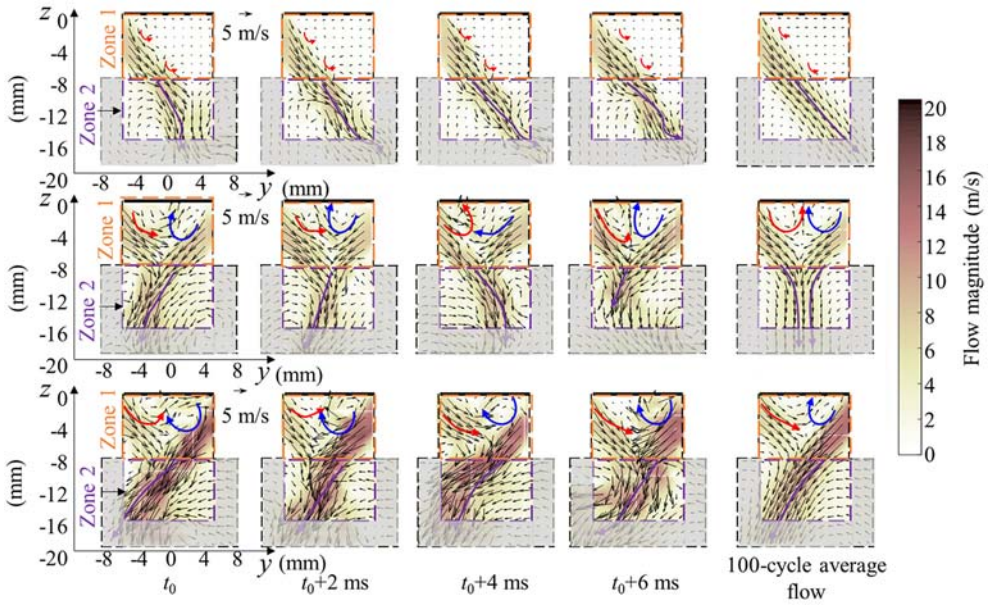

Figure 5. Consecutive snapshots and 100-cycle average flow under 5 vs 0 m/s (1st row), 5 vs 5 m/s (2nd row) and 5 vs 11 m/s (3rd row), (t_0 is randomly selected; flow fields are displayed at an interval of 5 vectors).

through individual snapshots. At time t_0 or t_0 +6 ms, the left jet is divided into two parts by overcoming the flow resistance from the right jet at the impingement point. As a result, an enhanced rotating motion is formed in zone 1. Note that the reverse situation can be found at time t_0 +4 ms, and the snapshot at time t_0 +2 ms represents the transition flow structure between these two situations. Below zone 1, zone 2 displays the overall mixing characteristic which is the downward development of a merged jet with fluctuations to the left or right side. Overall, the initial mixing occurs with vortices as both jets enter the flow domain. These vortices are alternately induced by the two jets and further enhance the overall mixing. The merged jet fluctuates from one side to the other side and its flow path is significantly changed compared with their initial jet directions. Under such conditions, the left jet is occasionally redirected by the right jet such as at t_0, and sometimes the right jet is redirected by left jet such as at t_0+4 ms. Compared to the snapshot at t_0+6 ms with the one at t_0, the flow behavior almost recurs periodically.

When further increasing the flow magnitude of the right jet to 11 m/s, as shown in Figure 5 (c), the flow path follows the direction of the right jet as expected. Under such strong air flow from the right jet, the left jet is significantly redirected towards the direction of the right jet, leading to a perpetual split of the left jet into two parts. In zone 1, part of the left jet is redirected to move upward and then is entrained by the right jet. In such a situation, a strong clockwise rotation trend (negative vorticity) is generated near the right jet. In zone 2, the left jet is merged into the right jet to follow the right jet path because the momentum of the left jet is almost totally lost. Such behavior demonstrates the dominance of the right jet in the merging flow pattern which is a direct effect of larger flow magnitude.

Overall, among the three test conditions, the behavior of the left jet is very different even though its bulk flow velocity remains the same. That means when the ambient air condition on the left jet is changed, the effect by the right jet on the left jet can be strong, intermediate, or minimum, which represents three different interaction levels. Therefore the KE dissipation must also occur at different levels during the impinging process. The KE dissipation of different interaction levels can be analyzed by comparing the KE values in specific zones. The 100-cycle average and standard deviation of specific KE inside individual zones and both zones are shown in Figure 6. The baseline condition of single jet demonstrates 20 % more specific KE in zone 2 than that in zone 1. This is because the jet expanding from zone 1 to zone 2 leads to kinetic energy distributed in a slightly larger space. However, for dual-valve condition of 5 vs 11 m/s, the difference of specific KE between the two zones is only 6 %. This is because during the interaction, part of the left jet remains inside zone 1. More interestingly for 5 vs 5 m/s condition, specific KE in zone 1 surpasses that in zone 2. Compared with the baseline condition, specific KE in zone 1 under 5 vs 5 m/s condition increases to be more than 2 times of that under single jet case. This illustrates the ambient gas entrainment in zone 1 becomes stronger, leading to more increase of specific KE in zone 1

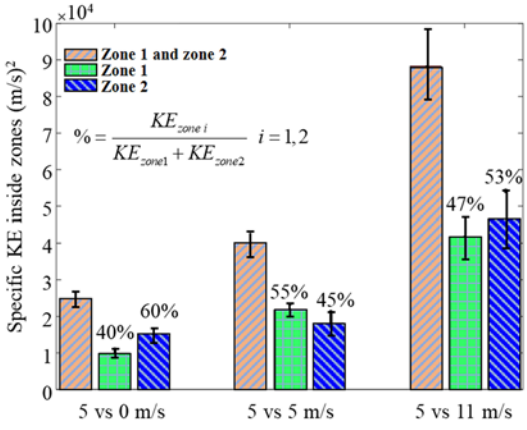

Figure 6. 100-cycle average and standard deviation of specific KE inside individual zones and combined zones.

over that in zone 2.

From the discussions above, the jet-to-jet interaction promotes enhanced entrainment motion in zone 1 and the flapping of merged jet direction in zone 2. The corresponding flow features can be best characterized using flow vorticity in zone 1 and merged jet angle in zone 2. These two parameters are important since the vorticity is related to the initial interaction strength between two impinging jets and the overall jet angle shows the downstream mixing characteristic of the merged jet penetration. Their physical meanings can be useful to elucidate the interaction process. Using the vorticity calculation, the flow features under three different interaction levels are quantified. In the left plot of Figure 7, the vorticity mapping shows the local rotating strength and the vectors show the jet direction of 100-cycle average flow. It is clear that for single jet condition, counterclockwise vorticity is always stronger than clockwise vorticity, resulting in a positive overall jet angle with an average of 26 degrees and a standard deviation of 6 degrees. This represents the flow behavior of a single jet naturally developing from the left valve. When both valves are open with comparable flow magnitude, as denoted in the 5 vs 5 m/s case, the positive vorticity

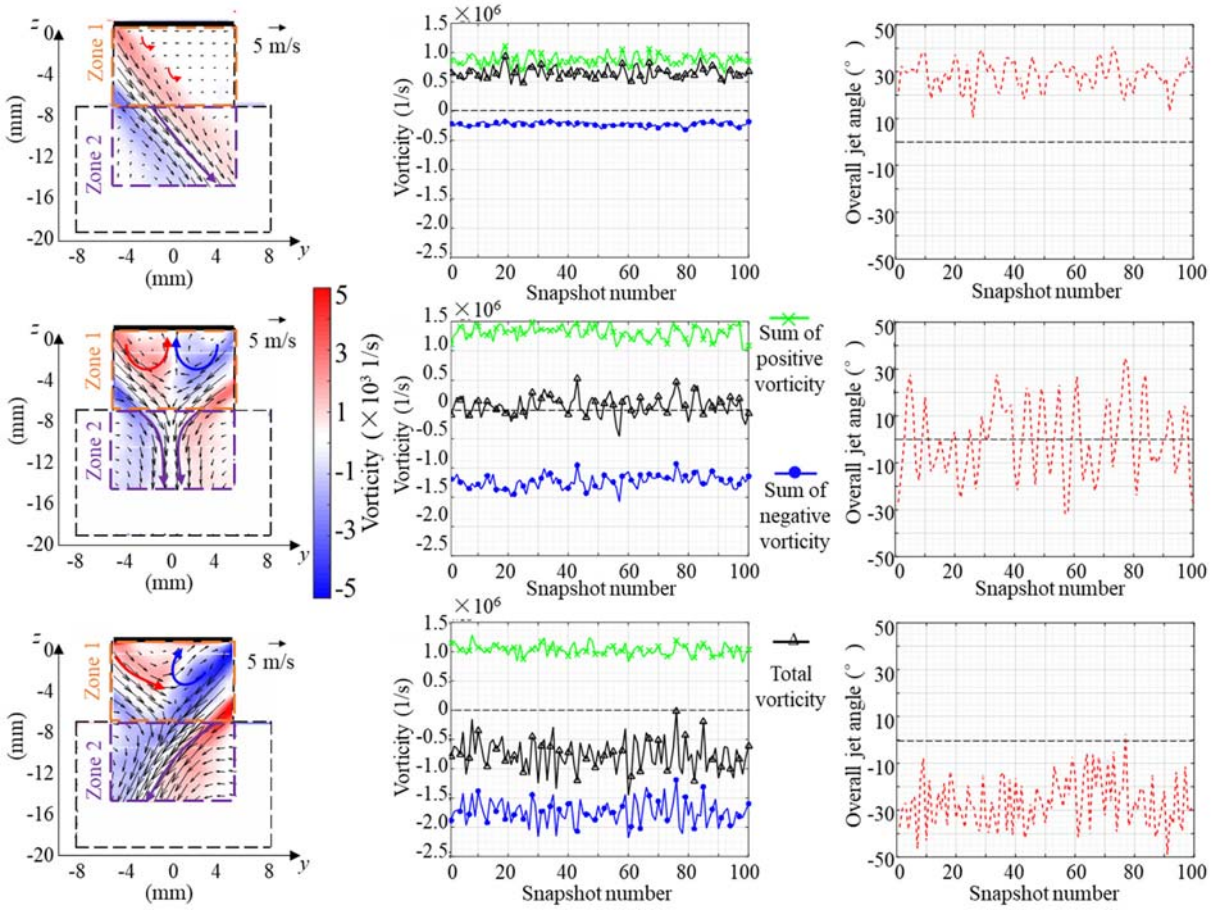

Figure 7. 100-cycle average flow structures overlaid by vorticity (left), vorticity variations in zone 1 (middle) and overall jet angle variations zone 2 (right) under 5 vs 0 m/s (1st row), 5 vs 5 m/s (2nd row) and 5 vs 11 m/s (3rd row).

becomes almost 1.6 times of that under the single valve condition. This demonstrates an enhanced positive vorticity under the ambient flow condition of an opposite jet relative to the left one. This is because the velocity gradient near the left jet increases when there exists an opposing right jet. From the corresponding vorticity mapping, the negative vorticity is mainly generated by the right jet. Since the strengths of two jets are comparable and the two jets are symmetrical around the middle section, the velocity gradient near the right jet is similar to that near the left jet. As a result, the magnitude of negative vorticity is comparable with the positive vorticity, which leads to that the total vorticity in the initial interaction zone 1 being around zero. In zone 2, the average of overall jet angle is also zero but with a larger standard deviation of 15 degrees. Compared with the single valve condition, the average overall jet angle is reduced from 26 degrees to 0 degrees. It is known that in the horizontal axis, the momentum magnitude of both jets is close to each other but their directions are opposite, while in the vertical axis, the momentum directions are the same when the two jets impinge. The horizontal momentum loss and the remaining momentum on the vertical direction make the merged jet confine along the vertical axis with an average of zero angle. The standard deviation of the overall jet angle around zero angle represents the fluctuations of jet angle to either the left or right side. The standard deviation under 5 vs 5 m/s is 2.5 times of that under single valve condition. This is caused by the strong competition of constant momentum exchange between two jets.

When the right jet continues to increase its strength, as denoted by 5 vs 11 m/s, the dominant vorticity and merged jet direction start to follow the right jet closely. It is found that even though the left jet strength is the same with that under the single-jet condition, the counterclockwise (positive) vorticity increases compared with the naturally developed jet. This is because the left jet is largely redirected by the right jet as seen in the corresponding vorticity mapping. Since the right jet strength is much higher than the left one, the magnitude of negative vorticity associated with the right jet is larger than positive vorticity with the left jet. Consequently, negative vorticity is dominant inside zone 1. In other words, the right jet dominates the flow feature in zone 1. In zone 2, the average of overall jet angle is estimated to be -27 degrees, whose magnitude is close to that for a single developed jet. The corresponding standard deviation is 11 degrees, which is almost two times of that under single valve condition but it is still less than that under 5 vs 5 m/s condition. The interaction level under 5 vs 11 m/s condition is between single jet (5 vs 0 m/s) condition and equal dual jets (5 vs 5 m/s).

The temporal analysis of flow features is further quantified by implementing the fast Fourier transform. The corresponding frequency spectrums are shown in Figure 8. For a naturally developed single jet condition, the frequency spectrum of vorticity in zone 1 does not show any local

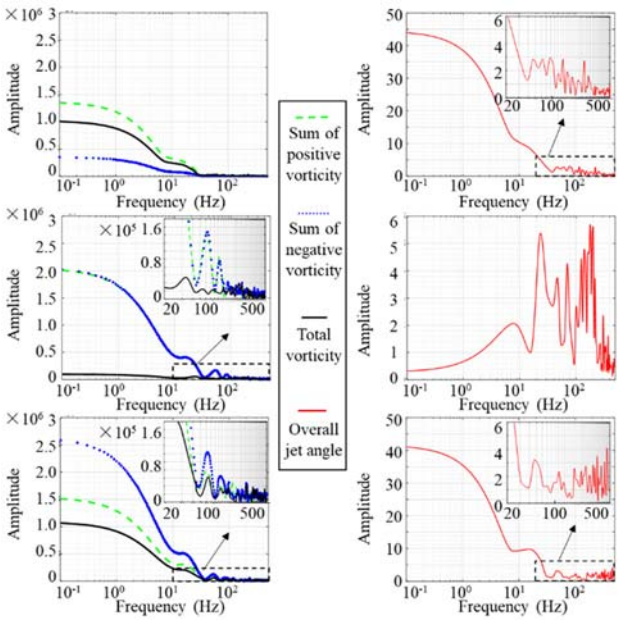

Figure 8. Frequency spectrums of vorticity variations in zone 1 (left) and overall jet angle variations in zone 2 (right) under 5 vs 0 m/s (1st row), 5 vs 5 m/s (2nd row) and 5 vs 11 m/s (3rd row).

dominant frequency. In zone 2, the frequency spectrum of overall jet angle exhibits several local dominant frequencies but the corresponding amplitude is low, which is likely due to random fluctuation. Different results are found in the dual-valve conditions. The amplitudes of local dominant frequencies become higher in both zones. Especially, the condition of 5 vs 5 m/s shows the largest amplitude among all three conditions, which means the quasi-periodical behavior is most obvious during the interaction of comparable jets. This finding agrees with the observation in individual snapshots. The reason behind this quasi-periodical behavior will be investigated later using POD method.

4.2. Linear Correlation of Vorticity and Overall Jet Angle

Since zone 1 and zone 2 are adjacent zones which represent the initial interaction and downstream mixing process accordingly, it is expected that flow characteristics of two zones have a strong correlation. Such correlation is displayed in Figure 9. Figure 9 (a) shows the vorticity distribution along with the jet direction based on the 100-cycle average flow and Figure 9 (b) illustrates the linear curve fit of flow vorticity and jet angle as a function of gas bulk flow velocity ratio. The R-square of the linear curve fit is almost 1.0 for both flow features. This finding demonstrates the gas bulk flow condition linearly affects the flow phenomena in both zones. It is clear to observe that when counterclockwise (positive) vorticity is dominant in zone 1,

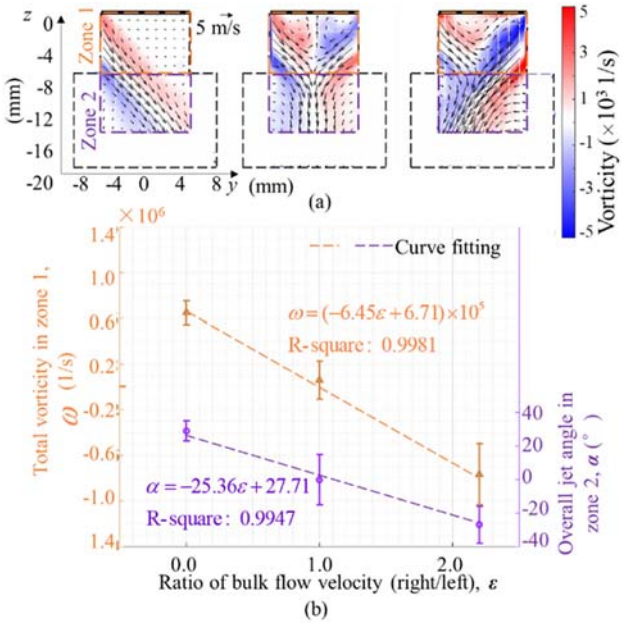

Figure 9. (a) Vorticity and average flow fields (flow fields are displayed at an interval of 5 vectors); (b) linear correlation of total vorticity and overall jet angle with the bulk flow velocity ratio.

the merged jet direction in the downstream zone 2 always points to the right side (positive value) and vice versa. When the bulk flow velocity ratio is 1.0, both the vorticity and overall jet angle are close to zero.

To further quantify the relationship between the two neighboring zones, the Pearson correlation coefficient is introduced since it is a good indicator to estimate the linear correlation between these two variables. Assuming the two variables are denoted by y_1 and y_2, the Pearson correlation coefficient ρ is calculated as follows:

$$\rho = \frac{\mathrm{cov}(y_1, y_2)}{\sigma_{y_1}\sigma_{y_2}} \tag{10}$$

where cov(y_1, y_2) is the covariance of y_1 and y_2, σ_{y_1} is the standard deviation of y_1, σ_{y_2} is the standard deviation of y_2. When ρ is 1.0, the two variables vary in exactly the same trend and they are strictly linearly correlated. When ρ is -1.0, the two variables vary in totally opposite trends. In this study, these two variables are total vorticity and overall jet angle, respectively. The correlation coefficient is found to be 0.98. That is, one zone is strongly linearly correlated with the other zone. Using such a linear correlation, if the vorticity behavior in zone 1 is known, the jet development in the downstream zone can be estimated and the dominant direction of momentum transfer can also be identified.

4.3. Underlying Flow Structures Using POD Analysis

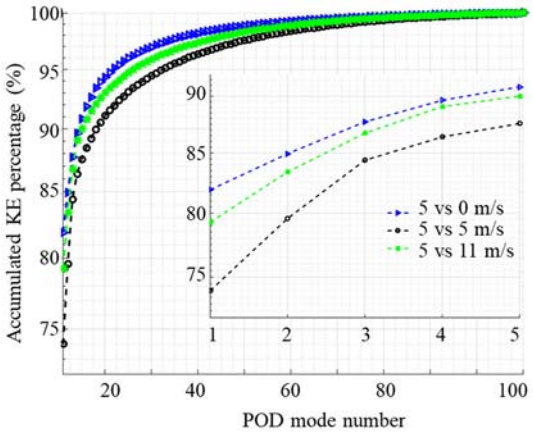

Figure 10. Accumulated KE percentage of all modes along with a magnified range of the first five modes.

POD is a powerful tool to extract the underlying structures and their kinetic energy percentages which provide another perspective to elucidate the interaction process as a result of jet impingement. Using 100 snapshots as inputs, 100 POD modes are achieved. These modes are arranged in the order of decreasing kinetic energy percentage based on their corresponding mode coefficients. Figure 10 displays the accumulated KE percentages. When comparing the same mode number, the single jet always shows the highest accumulated KE percentage among the three conditions. This is because there is less disturbance in the single jet formation process, resulting in a stable jet development. The dual-valve condition of 5 vs 5 m/s condition has the lowest accumulated KE percentage, which shows higher fluctuations under 5 vs 5 m/s condition. Since the first five modes have occupied more than 85 % kinetic energy of all modes, they can be used to demonstrate different interaction levels of the three conditions. Through the magnified plot, it is interesting to find that the 5 vs 11 m/s condition is closer to the single jet condition as mode number increases, while the 5 vs 5 m/s condition always shows a larger difference compared with the single jet.

It has been shown in Figure 10 that the first five modes, being the most energetic underlying structures for each case, show the difference among three interaction levels in terms of mode KE percentage. The corresponding reasons can be also explained using their mode structures, as displayed in Figure 11. For each condition, the first mode occupies the highest KE percentage because the first mode is always very close to the average flow structure. For other modes, the single jet presents multiple rotating structures around the jet path, which individually occupies a KE percentage of less than 3 %. These rotation structures are strongly correlated with the entrainment motion. Similar rotating structures around the jet path can be found in the modes 4 and 5 under the 5 vs 11 m/s condition. Either

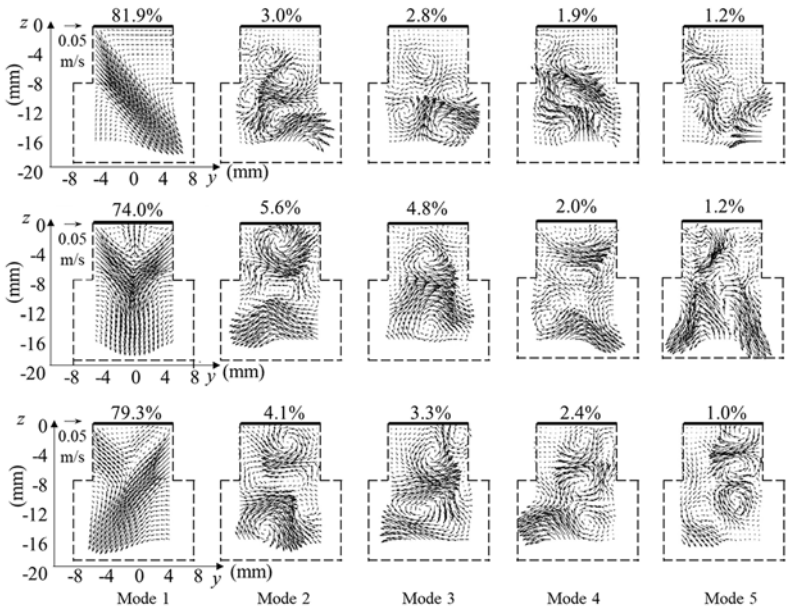

Figure 11. First five modes and corresponding KE percentages under 5 vs 0 m/s (1st row), 5 vs 5 m/s (2nd row) and 5 vs 11 m/s (3rd row), (modes are displayed at an interval of 3 vectors to display small-scale structures; percentage represents the kinetic energy percentage of each mode).

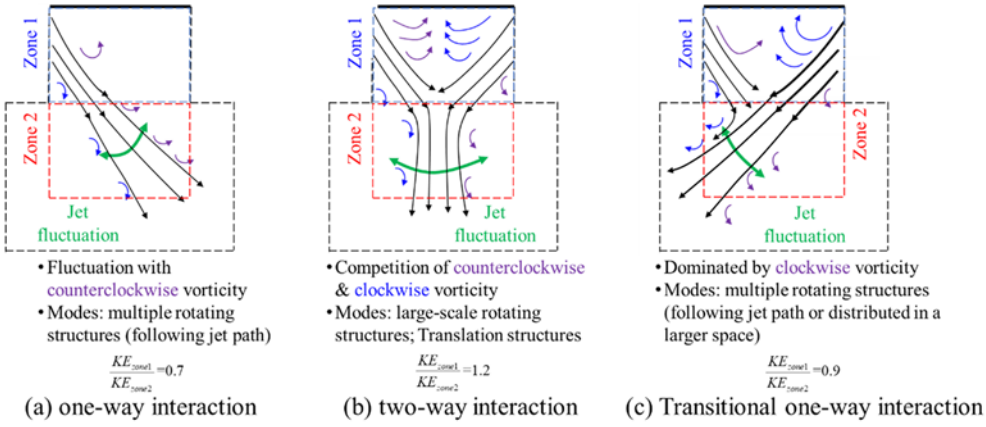

Figure 12. Characteristics of jet impingement-induced stability.

mode occupies a KE percentage of less than 3 %. This demonstrates that the 5 vs 11 m/s condition shows similar flow behavior as that in the single jet condition. The reason can be found by examining individual snapshots that the flow structure is dominated by the single right jet under 5 vs 11 m/s condition. When both jets are comparable in flow magnitude under the 5 vs 5 m/s condition, the modes display both translation structures and large-scale rotating structures rather than the small-scale rotating structures. These translation motions moving from one side to the other side can be found in zone 2 of mode 2, and around the interface between the two zones in mode 3, and again in both zones of mode 4. The large-scale rotation structures are found in zone 1 of modes 2 and 3. For modes 2 and 3, KE percentage of either mode occupies only around 3 %. That means these unique structures are the secondary dominant motions which are responsible for the quasi-periodical behavior under the 5 vs 5 condition.

For the 5 vs 11 m/s condition, modes 2 to 5 show multiple rotating flow structures. The rotating structures in modes 4 and 5 follow the jet path, while the structures in modes 2 and 3 are distributed in a larger space. These modes can be qualitatively separated into two groups based on their spatial features: modes 2 and 3 as the first group, and modes 4 and 5 as the second group. The second group is close to the features of single jet formation. For the first

group, each mode occupies about 3 % KE percentage and their rotating structures are very close to that in modes 2 and 3 under the 5 vs 5 m/s condition. Using the KE percentages and the similarity of the two mode groups, the interaction level under the 5 vs 11 m/s condition is between single jet condition and the 5 vs 5 m/s condition.

As shown in Figure 12, the single jet stability always results in a naturally developed single jet with minor fluctuations, which can be termed as one-way interaction. The case of 5 vs 5 m/s shows a stronger vorticity competition with largest jet angle fluctuations, which can be termed as two-way interaction. The case of 5 vs 11 m/s displays a flow behavior somewhat in between one-way and two-way interactions. Thus, the flow of the 5 vs 11 m/s condition is classified as transitional one-way interaction. The results of these three interaction levels show that there exists a strong linear correlation between the flow vorticity in zone 1 and merged jet angle in zone 2 as the bulk flow velocity ratio increases. It is found that different interaction levels of impingement-induced flow stability can affect the total KE distribution between the two adjacent zones. During two-way interaction the specific KE in zone 1 is more than that in zone 2 due to the enhanced entrainment motion in zone 1 and large KE dissipation in zone 2 by the strongest interaction when both jets impinge against each other. Using POD, the fluctuation of two-way interaction is found to be dominated by the large-scale rotating and translating structures. Such organized flow motions are responsible for the quasi-periodical behavior of two-way interaction.

5. CONCLUSION

In this study, three representative flow conditions were used to investigate the flow stabilities of impinging gas jets characteristics near valve exit. The primary findings can be made:

1) The jet-to-jet interaction process has been identified as one-way interaction, two-way interaction, and transitional one-way interaction. The two-way interaction process shows a strong KE dissipation from the initial interaction in zone 1 to the neighboring zone 2.
2) The flow vorticity and merged jet angle are identified as important parameters to characterize the flow phenomena in the neighboring zones because the dominant vorticity is directly controlling the initial interaction of the impinging jets and the merged jet behavior.
3) A strong spatial correlation between the flow vorticity and jet angle has been found. The competition of counterclockwise and clockwise vorticity in zone 1 causes the merged jet fluctuations in zone 2.
4) Two-way interaction shows multiple dominant local frequencies with the strongest vorticity competition in zone 1 and the largest fluctuations of jet direction in zone 2. Using POD analysis, the underlying large-scale rotating structures with translation are responsible for the quasi-periodical behavior of the two-way interaction.

ACKNOWLEDGEMENT–The PIV measurements were carried out at the National Engineering Laboratory for Automotive Electronic Control Technology of Shanghai Jiao Tong University. The experimental support and technical discussion by Prof. Min Xu and Prof. Xuesong Li from Shanghai Jiao Tong University are gratefully appreciated.

REFERENCES

Borée, J. and Miles, P. C. (2014). In-cylinder flow. *Encyclopedia of Automotive Engineering*, 1–31.

Brusiani, F., Falfari. S. and Cazzoli, G. (2014). Tumble motion generation in small gasoline engines: A new methodological approach for the analysis of the influence of the intake duct geometrical parameters. *Energy Procedia*, **45**, 997–1006.

Chatterjee, A. (2000). An introduction to the proper orthogonal decomposition. *Current Science* **78**, **7**, 808–817.

Chen, H., Reuss, D. L. and Sick, V. (2012). On the use and interpretation of proper orthogonal decomposition of in-cylinder engine flows. *Measurement Science and Technology* **23**, **8**, 085302.

Fogleman, M., Lumley, J., Rempfer, D. and Haworth, D. (2004). Application of the proper orthogonal decomposition to datasets of internal combustion engine flows. *J. Turbulence* **5**, **23**, 1–3.

Frapolli, N., Boulouchos, K., Wright, Y. M., Geiler, J. N., Manz, A. and Kaiser, S. A. (2019). Large Eddy Simulations and Tracer-LIF Diagnostics of Wall Film Dynamics in an Optically Accessible GDI Research Engine. *SAE Technical Paper No*. 2019-24-0131.

Ho, C. M. and Huerre P. (1984). Perturbed free shear layers. *Annual Review of Fluid Mechanics*, **16**, 365–424.

Hribernik, A., Bombek, G. and Fike, M. (2019). Phase-resolved PIV for investigating rotating stall within an axial fan. *Flow Measurement and Instrumentation*, **70**, 101659.

Ko, N. W. M. and Lau, K. K. (1989). Flow structures in initial region of two interacting parallel plane jets. *Experimental Thermal and Fluid Science* **2**, **4**, 431–449.

Lee, S. and Hassan, Y. A. (2018). Experimental study of flow structures near the merging point of two parallel plane jets using PIV and POD. *Int. J. Heat and Mass Transfer*, **116**, 871–888.

Li, H., Anand, N. K., Hassan, Y. A. and Nguyen, T. (2019). Large eddy simulations of the turbulent flows of twin parallel jets. *Int. J. Heat and Mass Transfer*, **129**, 1263–1273.

Li, Q., Page, G. J. and McGuirk, J. J. (2007). Large-eddy simulation of twin impinging jets in cross-flow. *The Aeronautical J.* **111**, **1117**, 195–206.

Liu, K., Haworth, D. C., Yang, X. and Gopalakrishnan, V. (2013). Large-eddy simulation of motored flow in a two-valve piston engine: POD analysis and cycle-to-cycle

variations. *Flow, Turbulence and Combustion* **91**, **2**, 373–403.

McTaggart-Cowan, G. P., Rogak, S. N., Munshi, S. R., Hill, P. G. and Bushe, W. K. (2010). The influence of fuel composition on a heavy-duty, natural-gas direct-injection engine. *Fuel* **89**, **3**, 752–759.

Nasr, A. and Lai, J. (2010). Applicability of Reichardt's hypothesis to the prediction of velocity field of multiple parallel plane jets. *J. Mechanics* **26**, **2**, N17–N22.

Ohm, I. Y. (2013). Effects of intake valve angle on combustion characteristic in an SI engine. *Int. J. Automotive Technology* **14**, **4**, 529–537.

Qin, W., Zhou, L., Liu, D., Jia, M. and Xie, M. (2019). Investigation of in-cylinder engine flow quadruple decomposition dynamical behavior using proper orthogonal decomposition and dynamic mode decomposition methods. *J. Engineering for Gas Turbines and Power* **141**, **8**, 081004.

Saghravani, S. F. and Ramamurthy, A. S. (2010). Penetration length of confined counter flowing free jets. *J. Hydraulic Engineering* **136**, **3**, 179–182.

Shim, Y. M., Sharma, R. N. and Richards, P. J. (2013). Proper orthogonal decomposition analysis of the flow field in a plane jet. *Experimental Thermal and Fluid Science*, **51**, 37–55.

Sivapragasam, M., Deshpande, M. D., Ramamurthy, S. and White, P. (2014). Turbulent jet in confined counterflow. *Sādhanā* **39**, **3**, 713–729.

Voisine, M., Thomas, L., Borée, J. and Rey, P. (2010). Spatio-temporal structure and cycle to cycle variations of an in-cylinder tumbling flow. *Experiments in Fluids* **50**, **5**, 1393–1407.

Wang, H., Lee, S., Hassan, Y. A. and Ruggles, A.E. (2016). Laser-Doppler measurements of the turbulent mixing of two rectangular water jets impinging on a stationary pool. *Int. J. Heat and Mass Transfer*, **92**, 206–227.

Xia, Q. and Zhong, S. (2017). Enhancement of inline mixing with lateral synthetic jet pairs at low Reynolds numbers: The effect of fluid viscosity. *Flow Measurement and Instrumentation*, **53**, 308–316.

Xu, M., Sun, Y. C., Cui, Y., Deng, K. Y. and Shi, L. (2016). One-dimensional model on fuel penetration in diesel sprays with gas flow. *Int. J. Automotive Technology* **17**, **1**, 109–118.

Yin, S., Fan, Y., Sandberg, M. and Li, Y. (2019). PIV based POD analysis of coherent structures in flow patterns generated by triple interacting buoyant plumes. *Building and Environment*, **158**, 165–181.